BODY-OF-REVOLUTION-ENHANCED IMAGING IN ULTRA-WIDEBAND SAR

Fu Lai Liang[*], **Qian Song, Han Hua Zhang, Tian Jin, and Zhi Min Zhou**

College of Electronic Science and Engineering, National University of Defense Technology, Changsha, Hunan 410073, P. R. China

Abstract—For ultra-wideband synthetic aperture radar (UWB SAR), there often exist a lot of clutters in the image, and the weak targets are easy to be masked by them. However, using the prior scattering knowledge of targets, enhanced imaging can be realized and beneficial improvements in image quality and detection performance can be expected. In this paper, an enhanced imaging method for body of revolution (BOR) has been researched. Since the BOR target has the unique feature of aspect-invariant characteristic, the aspect scattering entropy (ASE) is proposed to describe the diversity of aspect scattering and used in the BOR-enhanced imaging method. Then the application of the proposed method in landmine detection is discussed. The experimental results show that the BOR targets are effectively enhanced and the clutters are surpressed and thus the probability of landmine detection increases under the same false alarm rate.

1. INTRODUCTION

Ultra-wideband synthetic aperture radar (UWB SAR) has three characteristics that distinguish it from other sensors: low-frequency band, large bandwidth, and wide accumulated angle. These characteristics guarantee better soil or foliage penetration, higher resolution of SAR images, and richer aspect-dependent information of targets, making UWB SAR a promising method for detecting targets from a safe standoff distance [1–3].

A typical method for target detection can be divided into three steps: forming high resolution image, prescreening and discrimination [4]. The SAR image is the foundation of achieving

good performance for target detection. However, the traditional SAR imaging techniques have the following two drawbacks. Firstly, the traditional SAR image mainly reflects the intensity of targets. So the weak targets are easy to be masked by the strong clutters. Secondly, little prior knowledge of targets is used. So the targets are treated the same as the clutters [5, 6]. Thus, there exist a lot of clutters in the SAR image. These drawbacks make it a tough problem to detect weak targets based on the traditional SAR image. Aimed at this problem, the prior knowledge of targets contained in UWB SAR data should be brought into SAR imaging to enhance targets and suppress clutters. M. Cetin introduced the prior sparsity feature into SAR imaging and proposed an enhanced imaging method based on a regularized reconstruction [7, 8]. However, this method mainly focuses on the improvement of image resolution. Furthermore, its computation burden is very heavy and is not suitable for real-time processing. Unlike this method, this paper concentrates on the enhancement of the Body-of-Revolution (BOR), which is a typical weak target, and suppression of the clutters. And the used method should be in high efficiency.

BOR is a particular target with the axis of rotation perpendicular to the ground-plane. Many objects, such as the landmine and trunk, can be considered as BOR targets. As we know, the reflectivity of BOR is invariant with the aspect angle, which is called the aspect-invariant characteristic. While most of the clutters exhibit a strong dependence on the aspect angle and can be called anisotropy objects. UWB SAR has the wide aspect angle, which is usually over 45° and can be used to extract the aspect-invariant characteristic [9]. Subaperture technique is an efficient method to extract the aspect-dependent information [10–12] and used in this paper. Inspired by entropy, which is widely used to describe the sharpness of SAR images [13, 14], aspect scattering entropy (ASE) is proposed to measure the aspect-invariant feature. ASE of BOR is much larger than the anisotropy objects and not sensitive to the signal-to-noise ratio (SNR). In the following, a novel BOR-enhanced imaging method based on ASE and its application in landmine detection is proposed. The experimental results validate the effectiveness of the proposed method.

The paper is structured as follows. In Section 2, the aspect-invariant characteristic of BOR is analyzed. Then a metric of the aspect-invariant characteristic based on ASE is presented. Based on these discussions, in Section 3, an ASE-based BOR-enhanced imaging method is proposed. Application of the proposed method in landmine detection is discussed in Section 4. The effectiveness of the proposed method is demonstrated in Section 5 based on the airship-mounted

UWB SAR (AMUSAR) data. Finally, Section 6 summarizes the contributions of the paper.

2. ANALYSIS ON ASPECT-INVARIANT CHARACTERISTIC

2.1. Aspect-invariance Comparison of Different Objects

In traditional SAR imaging, the multi-aspect signatures are integrated to form a single image, thereby losing some of the explicit aspect dependence. In contrast, subaperture technique divides the collected returns into several subapertures, and then forms image with the aspect dependence preserved. Each subaperture image is formed using traditional SAR imaging techniques, but only represents the energy reflected from the ground patch over a limited range of aspect angles. Thus, a coregistered series of such subaperture images represent how the reflectivity of the ground patch images varies with respect to the aspect angle. A natural way of getting the aspect-dependent information of targets is to view a series of subaperture images as forming a collection of pixel trajectories. We expect that the pixels corresponding to BOR will not change across the sequence but pixels that correspond to anisotropy target will show significant variation across the sequence. In order to validate the above analysis, we resort to the electromagnetic simulation. The finite-difference time domain (FDTD) method for numerical calculation is an effective way to simulate data under various conditions for UWB SAR [15, 16]. We employ the FDTD method to simulate the scattering data of a cylinder and a trihedral. Obviously, the cylinder is a BOR target. According to [17], a cylinder with the similar size of landmine often yields two dominant scatterers in the range direction, which is called double-hump signature. As Fig. 1 shows, the pixels corresponding to the two dominant scatterers of cylinder exhibit aspect-invariant characteristic. Unlike the objects such as the dihedral, the trihedral changes slowly with the azimuth aspect. The 3 dB width of square trihedral is 25°, and the 3 dB width of the triangle trihedral is even up to 40°. And the aspect angle of antenna is narrow for high frequency band SAR, so the aspect dependence is not prominent. Thus, in conventional high frequency band SAR imaging, trihedral is often seen as an isotropic point scatterer. However, owing to the wide aspect angle of the low-frequency UWB SAR system, the fluctuation of the trihedral's scattering reflectivity with aspect angle can not be neglected. That means the approximation of isotropy point-like scatter seems not true any more. The electromagnetic simulation results in Fig. 1 can demonstrate the above analysis. In Fig. 1 the pixel corresponding to
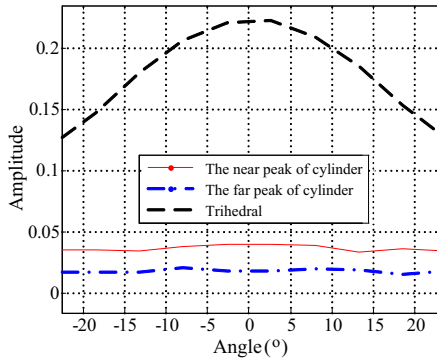
Figure 1. Comparison of aspect-dependent features using FDTD simulation data. The size of the trihedral is 0.3 m. The diameter and height of the cylinder are 0.3 m and 0.1 m, respectively.

the trihedral shows significant variation in aspect reflectivity.

It is well known that the radiation pattern of a real antenna exhibits anisotropy, i.e., the radiated fields are generally a function of the aspect angle. Consequently, if this effect is not compensated for, the aspect-dependent scattering fields will not only be a function of the aspect-dependent target signature, but also of the antenna pattern. The radiation pattern of antenna can be measured in dark rooms or estimated from real SAR data [18, 19]. Besides, since the range between the centre of each subaperture and the target is not constant in the strip-map SAR mode, the gain loss is induced. To solve the above problems, a rigorous radiometric calibration for each subaperture image would be needed. More details on the radiometric calibration can refer to [20].

2.2. Metric of Aspect-invariant Characteristic Based on ASE

Assume that the original full aperture is decomposed into a sequence of subaperture images $I_{i,j}^n$ $(n = 1, \ldots, N)$ corresponding to the aspect angles θ_n $(n = 1, \ldots, N)$. Where N denotes the number of subapertures, i and j represent the pixel index along the range and azimuth directions, respectively. The scattering phenomenology of each pixel is extracted from the subaperture images, yielding a sequence of aspect scattering vectors. Let $p_{i,j}^n$ be the proportion of $I_{i,j}^n$ in aspect scattering vector,

$$p_{i,j}^n = \left| I_{i,j}^n \right| \bigg/ \sum_{n=1}^{N} \left| I_{i,j}^n \right| \tag{1}$$

According to the definition of entropy [13], the metric of aspect-invariant characteristic is given as

$$M_{i,j} = -\sum_{n=1}^{N} p_{i,j}^n \ln(p_{i,j}^n) \qquad (2)$$

where $p_{i,j}^n$ satisfies $0 \le p_{i,j}^n \le 1$, so

$$0 \le M_{i,j} \le \ln N \qquad (3)$$

Only when $p_{i,j}^1 = p_{i,j}^2 \ldots = p_{i,j}^N = 1/N$, can $M_{i,j}$ achieve the maximum value. Ideally, only the pixels corresponding to BOR can attain the maximum value of $M_{i,j}$. Therefore, the BOR can be enhanced by (2) in theory. However, limited by the azimuth resolution of subaperture images, N is generally small. As a result, BOR and anisotropy targets may not be well distinguished using (2). Assume that the aperture collected from FDTD simulation is divided into 9 subapertures, the metrics of the near and far peaks of the cylinder and the trihedral using (2) are 2.1966, 2.1953 and 2.1619, respectively. To solve this problem, we have to find a nonlinear mapping function to enlarge the distinction. As discussed previously, the equation of $\ln N - M_{i,j} = 0$ holds only for the pixel corresponding to BOR target. Obviously, the reciprocal of $\ln N - M_{i,j}$ for BOR is an infinitely large quantity. So the range of $1/(\ln N - M_{i,j})$ is mapped to $[1/\ln N, +\infty)$. In other words, the difference between BOR and the anisotropy target is enlarged. (2) is further modified as

$$E_{i,j} = 1 \left/ \left[\ln N + \sum_{n=1}^{N} p_{i,j}^n \ln \left(p_{i,j}^n \right) \right] \right. \qquad (4)$$

The quantity defined in (4) is named as the aspect scattering entropy (ASE) in this paper. The influences of several factors on ASE are discussed as follows.
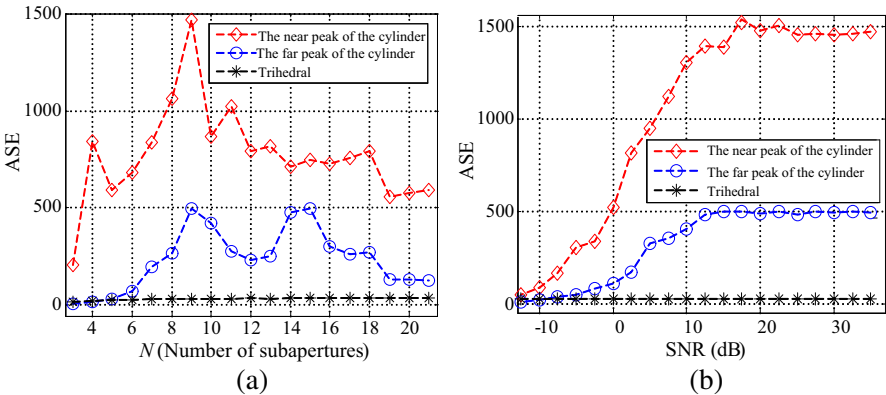
2.2.1. Number of Subapertures

Number of subapertures (N) is restricted by the required azimuth resolution of subaperture images and the expected BOR-enhanced property. Azimuth resolution is calculated as

$$\rho_A = \frac{\lambda_c}{4 \sin(\Phi_I/2N)} \qquad (5)$$

where λ_c denotes the wavelength corresponding to the central frequency, and Φ_I denotes the integration angle. Assuming that $\Phi_I = 45°$ and $\lambda_c = 0.2\,\text{m}$, N should not exceed 15 in order to get

an azimuth resolution of 2 m. And also small integration aperture will reduce SNR of subaperture image, which will degrade the precision of aspect-dependent feature extraction.

According to [17], for the two peaks of BOR, when one peak is well refocused, the other peak is defocused. The aspect-dependence information of the defocused peak, which is extracted from the defocused subaperture images, is not exact any more. As Fig. 2(a) shows, the ASE of the near peak of the cylinder keeps a large value. Although the ASE of the far peak of the cylinder is fluctuant due to the defocus problem mentioned above, it is much larger than the ASE of the trihedral for $N \geq 7$. When $N = 9$, the ASE of the near and far peak of cylinder are both maximum. In order to preserve the double-hump signature, $N = 9$ is selected and the corresponding subaperture angle width is about $5°$.

Figure 2. Influence of several factors on ASE. The integration angle is $-23°$ to $23°$. (a) Influence of N (number of subapertures) on ASE. (b) Influence of SNR on ASE ($N = 9$).

2.2.2. SNR

Influenced by noise, ASE of BOR is not an infinitely large value any more but a large value. In contrast, ASE of anisotropy target is a relatively small value. In order to analyze the influence of SNR, Gaussian white noise is added in FDTD simulation data. The simulation for every SNR is executed 30 times. Then the average is taken as the final result. As Fig. 2(b) shows, the ASEs of the targets increase as the SNR improves. But when SNR exceeds 15 dB, the ASEs keep stable. Especially, the ASEs of the two peaks of BOR are large enough even if SNR is 5 dB.

3. ASE-BASED BOR-ENHANCED IMAGING

3.1. Basic ASE-based BOR-enhanced Imaging Method

ASE is not sensitive to the scattering intensity of objects and ASE of BOR is much larger than the anisotropy targets. As a result, ASE is suitable for BOR-enhanced imaging. A direct idea of BOR-enhanced imaging is to use the ASE of each pixel as the final image instead of the traditional SAR image. However, in some applications the scattering intensity of objects may be needed for further processing since the scattering intensity can reflect difference of the material or size of the targets. Therefore, we preserve the scattering intensity of traditional SAR image in BOR-enhanced imaging. The BOR-enhanced imaging result is given as

$$I_{i,j}^E = I_{i,j} \cdot (E_{i,j})^\lambda \tag{6}$$

where $I_{i,j}$ is the traditional SAR image which is the superposition of subaperture images $I_{i,j}^n$, and λ is a variable which influences the extent of BOR enhancement. Generally, the selection of λ depends on the expected enhancement ratio of BOR and SNR of echo. Under a high SNR, λ could be set a large value to get better BOR-enhanced imaging effect. However, the aspect-invariant feature of some BOR targets maybe not prominent due to the uncertainties presented by a real system and the environment. Large λ may increase the missing alarm rate. In the practical applications, λ should be seriously selected to balance the BOR-enhanced imaging performance and the robustness. According to our experience $\lambda = 1$ can satisfy the common requirement.

The flow of the basic ASE-based BOR-enhanced imaging method (ASEBOREI) is given in Fig. 3. The aperture is uniformly divided into subapertures, and each subaperture image is formed using the traditional back-projection (BP) algorithm [5, 21]. These subaperture images are linearly integrated to form traditional SAR image, in which the reflectivity of trihedral is much stronger than cylinder. Thus, to detect cylinder in the traditional SAR image is a hard job since the strong clutters, i.e., trihedral, will disturb the cylinder. ASE of cylinder is much larger than trihedral in ASE image. The BOR-enhanced image is attained by (6) when $\lambda = 1$. The cylinder is effectively enhanced by the proposed method.

3.2. Considerations about Real Data

In real data, there are lots of clutters and noises, which will cause artificial targets without appropriate processing. Thus, the following conditions are under consideration in this section.

ASE image

Subapture images

(•)^λ

BOR-enhanced image

Conventional SAR image
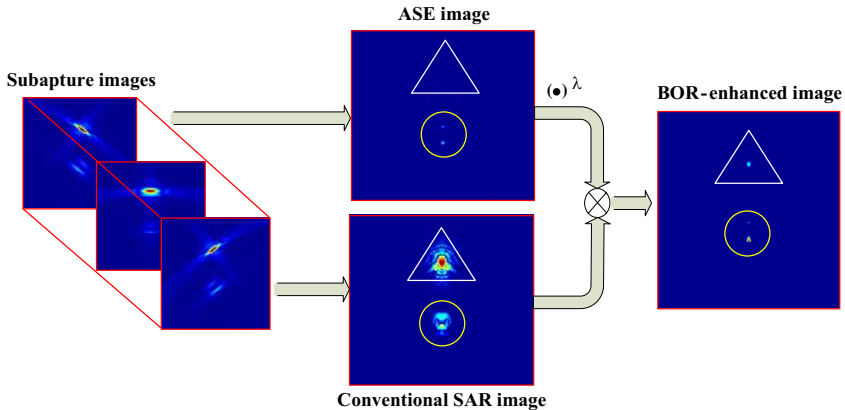
Figure 3. Flow of the basic ASEBOREI method. The data were generated by the FDTD simulation. The frequency bandwidth is 2 GHz, from 0.5 GHz to 2.5 GHz. The elevation angle is 60°, the aspect angle is from −23° to 23°. In the scene, a cylinder and a 0.3 m trihedral are placed, and the distance between the two targets is 1.414 m. The diameter and height of the cylinder are 0.3 m and 0.1 m. The cylinder and trihedral are marked in circle and triangle, respectively.

3.2.1. Strong Clutters with Small ASE

In order to preserve the differences between kinds of BORs, we introduce the traditional SAR image into the basic ASE-based BOR-Enhanced method. However, some anisotropy but strong clutters, such as the wall corner, may not be well suppressed due to their large amplitude in traditional SAR image. We prefilter the ASE image as

$$E_{i,j} = \begin{cases} E_{i,j}, & E_{i,j} >= T \\ 0, & E_{i,j} < T \end{cases} \qquad (7)$$

where T is the threshold of the prefilter. Generally, the value of T should be selected according to practical applications. For BOR-enhanced imaging in the urban region, T should be set a larger value so that the enhanced method can suppress the clutters, i.e., the wall corner, more effectively. For usual applications, T need not be set too large since a few of BOR targets possibly exhibit small ASE affected by complex environment. According to the analysis of the real data collected by the airship-mounted UWB SAR (AMUSAR) system [9], the ASEs of typical anisotropy clutters are less than 15. Especially for the targets similar to the dihedral, the ASEs are even below 3. In this paper, we set T to be 3 and that already satisfies our processing purpose.

3.2.2. Weak Clutters with Large ASE

Some weak clutters or noises, such as small round rocks, may happen to exhibit strong aspect-invariant feature. Thus, they would be enhanced to some extent and make bright points in the BOR-enhanced image. Small λ may help for the alleviation of the above problem. Since the weak clutters and the noises with large ASE come out randomly, the sizes of them in BOR-enhanced image are usually small. Morphological filter utilizing the differences in size is suitable for suppression of them. In recent researches on detection of weak and small targets, morphological filter is often used as an efficient way of clutter reduction and is put in the prescreening step [22]. Thus, morphological filter is not included in our BOR-enhanced imaging method.

3.3. Processing Steps

The main processing steps of ASEBOREI are shown as follows.

Step **1.** The subaperture image $I_{i,j}^n$ corresponding to each observation angle θ_n is formed based on subaperture technique.

Step **2.** ASE of each pixel is calculated using (4).

Step **3.** ASE image $E_{i,j}$ is prefiltered to remove the clutters with small ASE below the threshold.

Step **4.** The high resolution SAR image is formed by coherently adding the subaperture images together.

*Step* **5.** The high resolution SAR image is weighted by $(E_{i,j})^\lambda$.

3.4. Computational Burden

The main computation burden of ASEBOREI is from the subaperture algorithm and computation of ASE. Assuming the image grid is $M \times M$, the length of aperture is M and the number of subapertures is N. The computation burden of BP and Factorized Fast Back Projection (FFBP) are $O(M^3)$ and $O(M^2 \log M)$ respectively [23]. The computation cost of subaperture imaging is the same as the BP algorithm. The computation cost of ASE is $O(M^2 N)$. Because N is usually small, the ASE computation cost is close to FFBP and much lower than BP. Therefore, ASEBOREI has low additional computation burden and is suitable for practical applications.

4. APPLICATIONS IN LANDMINE DETECTION

Landmine detection is a tough problem of weak and small targets detection in strong clutter environment [24–26]. As a typical BOR target, landmine will be enhanced by ASEBOREI. The details of

ASEBOREI have been given in Section 3. Fig. 4 gives the flow of landmine detection. As we can see, ASEBOREI is done on original SAR echo at first. Then the prescreening is adopted, which contains constant false alarm rate (CFAR) [27], morphological filtering, and clustering. At last, landmine is discriminated via ROI extraction and classifying.
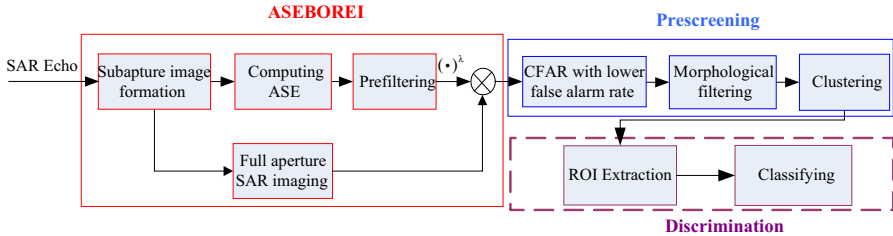
Figure 4. Flow of landmine detection based on ASEBOREI.

In traditional landmine detection, it is hard to get high detection probability and low false alarm rate simultaneously. To guarantee the personnel safety, a high detection probability is necessary. But it will lead to high false alarm rate too. However, ASEBOREI step guarantees the high detection probability under a lower false alarm rate in our method, so CFAR with lower false alarm rate is adopted.

As discussed in Section 3, some clutters and noises which happen to exhibit aspect invariance are also enhanced to some extent. Since they occur randomly, bright points caused by them are often small-sized. Therefore, morphological filtering is suitable to remove them. Besides, the clutters with large size can also be removed by morphological filtering. Therefore, the morphological filtering is used on CFAR result. The details of morphological filtering are given in [22]. Clustering is adopted after morphological filtering for acquiring the centres of landmines which are used to extract region of interest (ROI). Each ROI extracted from the entire SAR image contains a suspected object. The following discrimination stage is to classify those suspected objects into targets and nontargets.

Because the prior information is used in SAR imaging, there exist few false alarms in image after prescreening, and naturally the computation burden of landmine discrimination will be reduced. If enough information is utilized in landmine enhanced imaging, the discrimination processing can be left out.

5. RESULTS

The data are collected by the AMUSAR system which provides surveillance of large areas via a strip-map SAR mechanism [9]. Fig. 5 shows the photos of the system. The AMUSAR system operates over the frequency range from 0.5 GHz to 2.5 GHz. The airship flies at 100 meters above ground when the AMUSAR is working. The integration angle is 45° and the aperture is uniformly divided into 9 subapertures.


Figure 5. Photos of the AMUSAR system.

5.1. Validation of Enhanced Imaging for BOR

Since BOR detection is a problem of one-class classification [28], all the objects except BOR are recognized as clutters. Analysis on all kinds of clutters is difficult and time-consuming, among which the trihedral is the most typical and significant one. Firstly, the trihedral is widely used and usually seen as a basic model to construct the complicated objects. Secondly, the reflectivity of trihedral is strong and changes slowly with the aspect angle. The proposed method is mainly based on aspect-invariance and reflectivity intensity, thus the trihedral is very difficult to be suppressed. In other words, if the proposed method is valid for suppression of trihedral, most of the other clutters can also be suppressed. So we choose the trihedral as the reference object to show the performance of the proposed method.

As shown in Fig. 6, region A is an even and smooth road. Four targets, including a landmine and three 0.3 m trihedral reflectors, are disposed in region A along the flight direction. The distance between them is 5 m. The region B is uneven ground full of rocks and grass.

The experimental results show that ASEBOREI has the following two advantages.

(a)   (b)
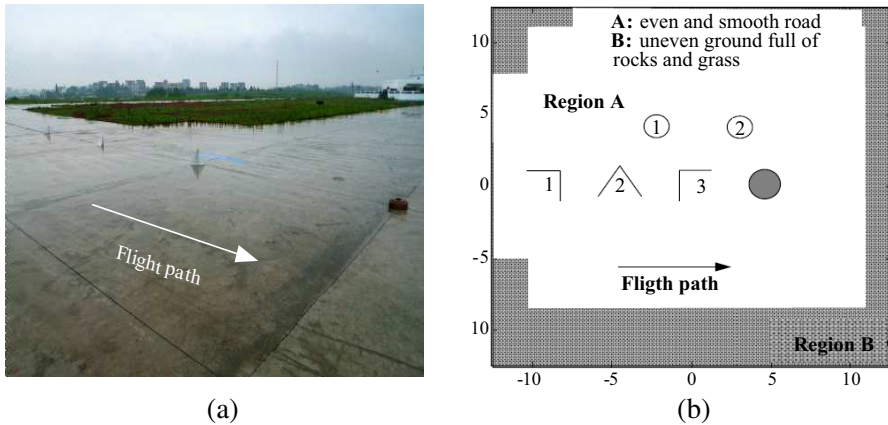
'⬤' denotes the landmine and '1⌐', '2⟩', '3⌐' denote three trihedrals whose pose angles are southeast 45°, south and southwest 45°. '①' and '②' denote two round holes).

Figure 6. Experiment scene. (a) The photo of the scene. The flight path is from the east to the west. (b) Schematic diagram of the target distribution.

5.1.1. Enhancing the BOR Target Effectively

As shown in Table 1, in traditional SAR image the landmine is much weaker than trihedral-2, but close to trihedral-1. Therefore, discrimination of landmine from trihedral by reflectivity intensity is very hard. Owing to the diversity of aspect-dependent feature the ASE of landmine is much larger than the trihedrals. The landmine is enhanced by 17 dB by ASEBOREI. As a result, ASEBOREI is effective in BOR enhancement.

Table 1. Analysis on the ASEBOREI results.

	Traditional SAR image (dB)	ASE	ASEBOREI result (dB)
Landmine	−10.18	189.42	7.09
Trihedral-1	−12.74	3.70	−18.08
Trihedral-2	0	13.83	0
Trihedral-3	−6.65	4.50	−15.57
Hole-1	−19.49	40.60	−10.20
Hole-2	−21.31	19.01	−18.55

5.1.2. Suppressing the Sidelobe, Noise and Clutters, so as to Improve Image Quality

Due to the double-hump signature of landmine, we choose trihedral-2 to analyze the sidelobe suppression effect (marked as region C1 and region C2). As Fig. 7 shows, the sidelobe of trihedral-2 is suppressed effectively in region C2. The azimuthal integral sidelobe ratio (ISLR) of trihedral-2 is reduced from $-12.9658\,\text{dB}$ to $-20.5158\,\text{dB}$.

The primary components of image in region A are thermal noise of SAR system, quantization noise and aliasing component of close targets. The variance of D1 is 0.0066, but the variance of D2 is reduced to $1 \cdot 6202 \times 10^{-5}$. The above result shows that ASEBOREI has the ability of noise suppression.

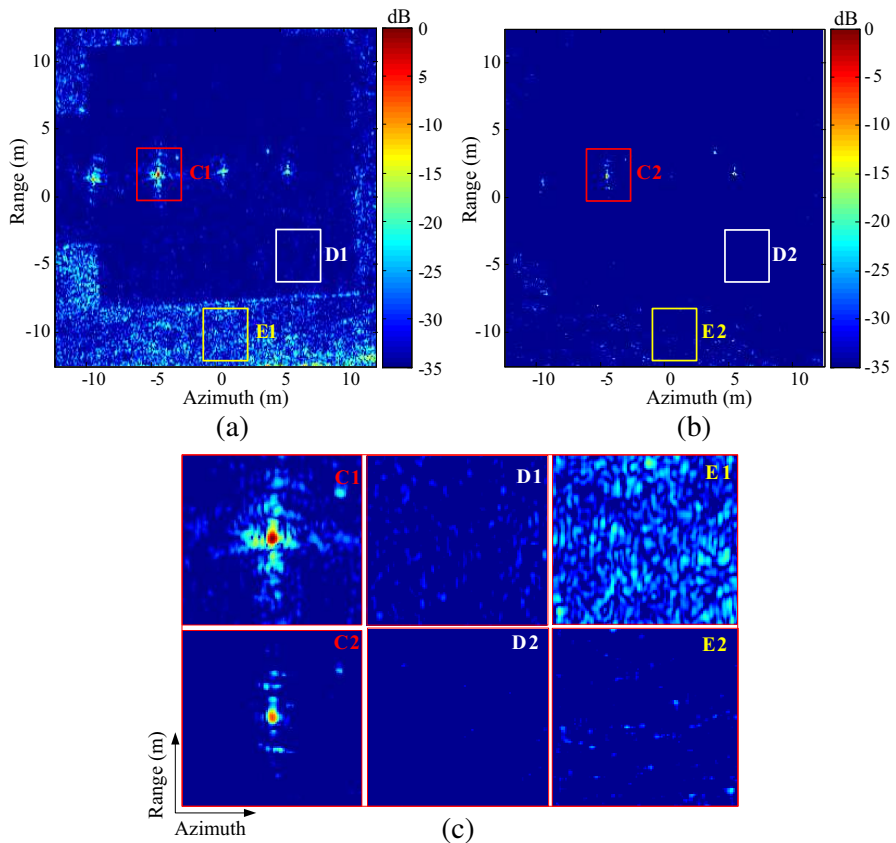ASEBOREI can also suppress the clutters owing to the aspect-

Figure 7. Results of the simple scene. (a) Traditional SAR image. (b) ASEBOREI result. (c) Comparison of typical regions.

dependent characteristic of the clutters. There exist lots of clutters in region B of the scene. Take the comparison of region E1 and E2 as an example. The average amplitude value of region E1 attains 0.3973, but the average amplitude value of E2 is only 0.0126.

5.2. Improvement for Landmine Detection Performance

The landmines used in the experiment are antitank landmines with diameter of 30 cm and all the landmines are shallow buried. The water content of soil is between 5% and 10% in weight. There are 40 landmines placed in the minefield (as shown in Fig. 8). A truck stops outside of the minefield at a distance of 35 m. Four metal top hats which are 0.3 m high and 0.3 m diameter are also placed in the scene.
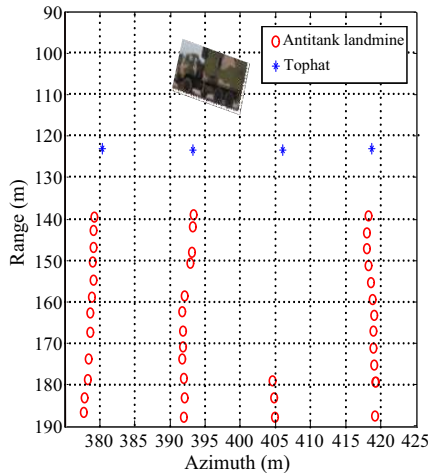

Figure 8. Distribution of the targets.

Figure 9 gives the comparison of traditional SAR image and ASEBOREI result. Fig. 9(a) shows that the truck in the traditional SAR image is much stronger than the landmines. And its azimuth sidelobe is prominent due to the asymmetry of accumulation aperture. And also there are many strong clutters in SAR image which may cause false alarms. In Fig. 9(b), the SAR image is much cleaner. Especially, the truck is effectively suppressed and the landmines are more prominent. However, the tophats are also enhanced since they are BOR targets and their amplitudes are similar as or even higher than the landmines. To solve this problem, more prior information, i.e., the frequency-dependent information, is needed. However, this is the future research and not included in this paper.
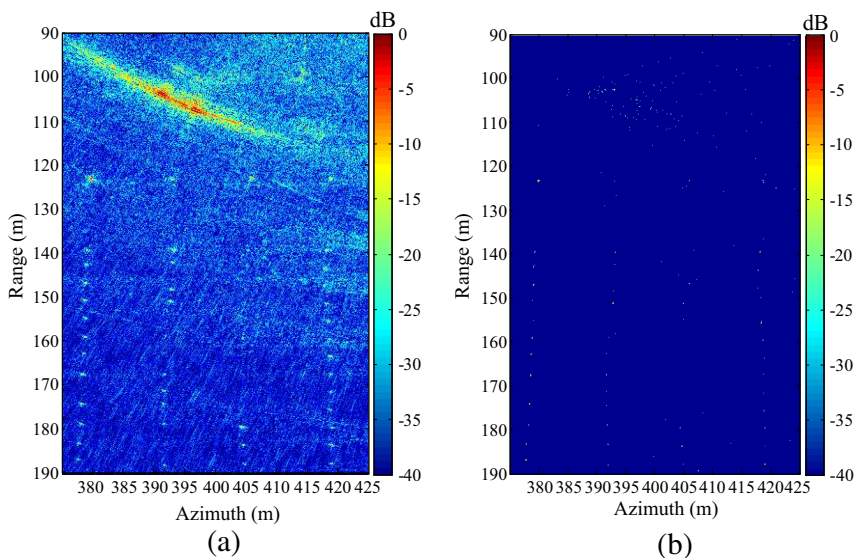
Figure 9. Comparison of traditional SAR image and ASEBOREI result. (a) Traditional SAR image. (b) ASEBOREI result ($\lambda = 1$).
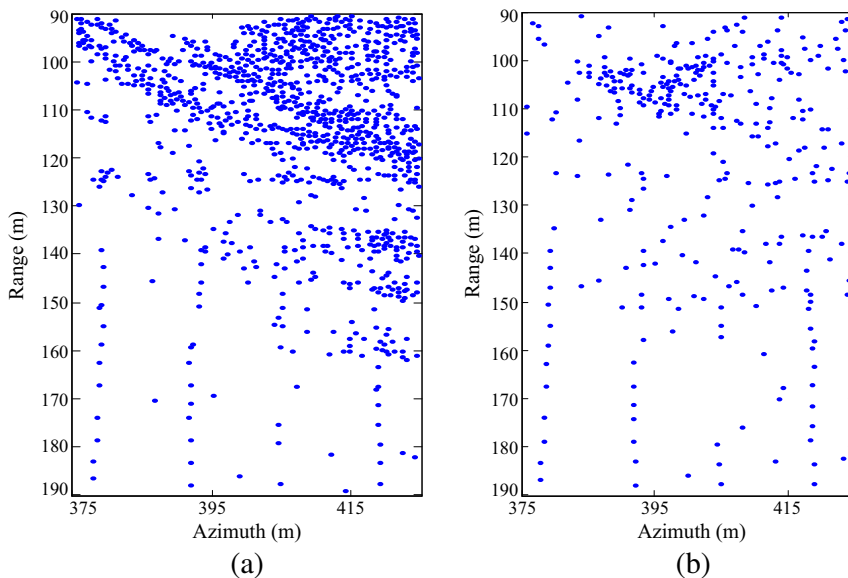
Figure 10. Prescreening results when the parameter of false alarm rate in CFAR detector is 0.001. (a) Prescreening result based on the traditional SAR image. (b) Prescreening result based on the ASEBOREI result ($\lambda = 1$).

Figures 10(a) and 10(b) are results of prescreening. It can be seen that there are more false alarms in detection image based on traditional SAR image than the ASEBOREI result. For acquiring more accurate conclusions, the receiver operator characteristic (ROC) curves are adopted. The false alarm rate used in Fig. 11 is the false alarm rate of CFAR. The detection is executed ten times. Then the average is taken as the final result. As we can see, the performance of landmine detection is affected by λ. The larger is λ, the steeper is the ROC curve. However, in the complicated scene the landmine may be influenced by strong clutters such as the rocks or grass. Then the aspect-invariant feature of some landmines is not prominent any more. It is not suitable to select too large λ in such case. In this experiment, one landmine is lost when $\lambda = 1.5$. In this paper, λ is selected to be 1 to balance the performance of landmine-enhanced imaging and the robustness.
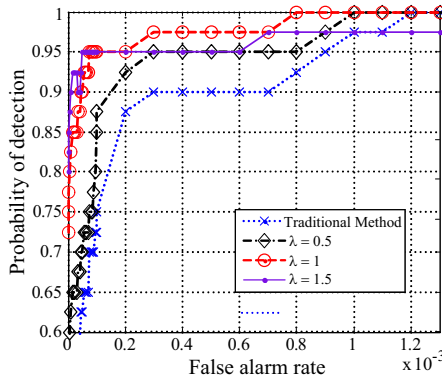
Figure 11. ROC curves for different values of λ.

6. CONCLUSIONS

In this paper, a novel idea of enhanced imaging is introduced by applying the prior knowledge of targets to SAR imaging. We focus on the enhanced-imaging of BOR targets since many objects such as the landmine and trunk can be considered as BOR targets. Then the aspect-invariant feature of BOR is integrated in BOR-enhanced imaging by the ASE. Furthermore, we apply the BOR-enhanced imaging to landmine detection. The experimental results show that the proposed method has the advantages of enhancing BOR targets and suppressing the clutters, sidelobe and noise. Owing to these advantages, the probability of landmine detection based on the BOR-enhanced imaging increases under the same false alarm rate compared

with the traditional landmine detection method. The strong point scatterers near the landmines will influence the extraction of the aspect-dependence characteristic. The method to reduce the influence is to improve the resolution of the subaperture images, since the energy from landmine and clutter are separated in high resolution image. Some feature exaction methods based on the space-wavenumber distribution (SWD) can exact the aspect angle invariance feature while maintain high spatial resolutions. The super-resolution imaging methods or compressive sensing (CS) can also be adopted to form subaperture images to improve the azimuth resolution with increased computation burden. These methods may be helpful to resolve the interference problem of strong clutters. The extensions of our BOR-enhanced imaging scheme to general target-enhanced imaging problems are possible. The only jobs are to select the appropriate feature and modify ASE to other metric indicators.

ACKNOWLEDGMENT

REFERENCES

1. Yang, J., X. Huang, T. Jin, J. Thompson, and Z. Zhou, "Synthetic aperture radar imaging using stepped frequency waveform," *IEEE Transactions on Geoscience and Remote Sensing*, Vol. 50, 2026–2036, 2012.

2. Andrieu, J., F. Gallais, V. Mallepeyre, V. Bertrand, B. Beillard, B. Jecko, et al., "Land mine detection with an ultra-wideband SAR system," *Proc. SPIE*, Vol. 4742, 237–247, 2002.

3. Vickers, R. S., "Design and applications of airborne radars in the VHF/UHF band," *IEEE Aerospace and Electronic Systems Magzine*, Vol. 47, 26–29, 2002.

4. Ratto, C. R., P. A. Torrione, and L. M. Collins, "Exploiting ground-penetrating radar phenomenology in a context-dependent framework for landmine detection and discrimination," *IEEE Transactions on Geoscience and Remote Sensing*, Vol. 49, 1689–1699, 2011.

5. Rau, R. and J. H. Mcclellan, "Analytic models and postprocessing techniques for UWB SAR," *IEEE Transactions on Aerospace and Electronic Systems*, Vol. 36, 1058–1074, 2000.

6. Lorenzo, J. A., F. Quivira, and C. M. Rappaport, "SAR imaging of suicide bombers wearing concealed explosive threats," *Progress In Electromagnetics Research*, Vol. 125, 255–272, 2012.

7. Cetin, M., W. C. Karl, and D. A. Castanon, "Evaluation of a regularized SAR imaging technique based on recognition-oriented features," *Proc. SPIE*, Vol. 4053, 40–51, 2000.

8. Cetin, M. and W. C. Karl, "Feature-enhanced SAR image formation based on noquadratic regularization," *IEEE Transactions on Image Processing*, Vol. 10, 623–631, 2001.

9. Song, Q., H. H. Zhang, F. L. Liang, Y. H. Li, and Z. M. Zhou, "Results from an airship-mounted ultra-wideband synthetic aperture radar for penetrating surveillance," *2011 Asia-Pacific Conference on Synthetic Aperture Radar*, 1–4, Seoul, Korea, 2011.

10. Ji, S. H., R. Parr, and L. Carin, "Nonmyopic multiaspect sensing with partially observable Markov decision processes," *IEEE Transactions on Geoscience and Remote Sensing*, Vol. 55, 2720–2730, 2007.

11. Wang, T., J. M. Keller, and P. D. Gader, "Frequency subband processing and feature analysis of forward-looking ground-penetrating radar signals for land-mine detection," *IEEE Transactions on Geoscience and Remote Sensing*, Vol. 45, 718–729, 2007.

12. Tan, C.-P., J.-Y. Koay, K.-S. Lim, H.-T. Ewe, and H.-T. Chuah, "Classification of multi-temporal SAR images for rice crops using combined entropy decomposition and support vector machine technique," *Progress In Electromagnetics Research*, Vol. 71, 19–39, 2007.

13. Matthias, D. and M. Abbe, "A history of graph entropy measures," *Information Sciences*, 57–78, 2011.

14. Sjoberg, D., "On uniqueness and continuity for the quasi-linear, bianisotropic Maxwell equations, using an entropy condition," *Progress In Electromagnetics Research*, Vol. 71, 317–339, 2007.

15. Zhang, Y.-Q. and D.-B. Ge, "A unified FDTD approach for electromagnetic analysis of dispersive objects," *Progress In Electromagnetics Research*, Vol. 96, 155–172, 2009.

16. Hu, X.-J. and D.-B. Ge, "Study on conformal FDTD for electromagnetic scattering by targets with thin coating," *Progress In Electromagnetics Research*, Vol. 79, 305–319, 2008.

17. Jin, T. and Z. M. Zhou, "Feature extraction and discriminator design for landmine detection on double-hump signature in ultra-wideband SAR," *IEEE Transactions on Geoscience and Remote*

Sensing, Vol. 46, 3783-3791, 2008.

18. Zhang, P.-F., S.-X. Gong, and S. F. Zhao, "Fast hybrid FEM/CRE-UTD method to compute the radiation pattern of antennas on large carriers," *Progress In Electromagnetics Research*, Vol. 89, 75–84, 2009.

19. Guarnieri, A. M. and D. D. Aria, "Wide-angle azimuth antenna pattern estimation in SAR images," *2003 International Geoscience and Remote Sensing Symposium*, Vol. 5, 3105–3107, 2003.

20. Zyl, J. J., "Calibration of polarimetric radar images using only image parameters and trihedral corner reflector responses," *IEEE Transactions on Geoscience and Remote Sensing*, Vol. 28, 337–348, 1990.

21. Capozzoli, A., C. Curcio, and A. Liseno, "Fast GPU-based interpolation for SAR backprojection," *Progress In Electromagnetics Research*, Vol. 133, 259–283, 2013.

22. Pham, Q. H., T. M. Brosnan, M. J. T. Smith, and R. M. Mersereau, "A morphological technique for clutter suppression in ATR," *SPIE Conference on Automatic Target Recognition VIII*, Vol. 3374, 367–374, Orlando, Florida, 1998.

23. Ulander, L. M., H. Hellsten, and G. Stenström, "Synthetic-aperture radar processing using fast factorized back-projection," *IEEE Transactions on Aerospace and Electronic Systems*, 760–776, 2003.

24. Jin, T. and Z. Zhou, "Ultrawideband synthetic aperture radar landmine detection," *IEEE Transactions on Geoscience and Remote Sensing*, Vol. 45, 3561–3573, 2007.

25. Wang, Y., Q. Song, T. Jin, Y. Shi, and X.-T. Huang, "Sparse time-frequency representation based feature extraction method for landmine discrimination," *Progress In Electromagnetics Research*, Vol. 133, 459–475, 2013.

26. Lou, J., T. Jin, and Z. Zhou, "Feature extraction for landmine detection in UWB SAR via SWD and ISOMAP," *Progress In Electromagnetics Research*, Vol. 138, 157–171, 2013.

27. Habib, M. A., M. Barkat, B. Aissa, and T. A. Denidni, "Ca-CFAR detection performance of radar targets embedded in 'non centered Chi-2 Gamma' clutter," *Progress In Electromagnetics Research*, Vol. 88, 135–148, 2008.

28. Tax, D., "One-class classification: Concept-learning in the absence of counter-examples," Ph.D. Thesis, Deflt University of Technology, 2001.